Durability of aligned microtubules dependent on persistence length determines phase transition and pattern formation in collective motion

Hang Zhou,[1] Wonyeong Jung,[2,†] Tamanna Ishrat Farhana,[1,‡] Kazuya Fujimoto,[1] Taeyoon Kim,[2] and Ryuji Yokokawa[1]*

[1]Department of Micro Engineering, Kyoto University, Kyoto daigaku-katsura, Nishikyo-ku, Kyoto 615-8540, Japan

[2]Weldon School of Biomedical Engineering, Purdue University, West Lafayette, IN 47907, USA

[†]Present Address: Ragon Institute of MGH, MIT, and Harvard, Cambridge, MA 02139, USA

[‡]Present Address: Department of Sciences and Humanities, Military Institute of Science and Technology, Mirpur Cantonment, Dhaka 1216, Bangladesh

*Corresponding Author

Email: yokokawa.ryuji.8c@kyoto-u.ac.jp

Tel/Fax: +81-75-383-3680

ABSTRACT

Collective motion is a ubiquitous phenomenon in nature. The collective motion of cytoskeleton filaments results mainly from dynamic collisions and alignments; however, the detailed mechanism of pattern formation still needs to be clarified. In particular, the influence of persistence length, which is a measure of filament flexibility, on collective motion is still unclear and lacks experimental verifications although it is likely to directly affect the orientational flexibility of filaments. Here, we investigated the collective motion of microtubules with different persistence lengths using a microtubule-kinesin motility system. We showed that local interactions between microtubules significantly vary, depending on their persistence length. We demonstrated that the bundling of microtubules is enhanced by more durable alignment, rather than by more likelihood of alignment. An agent-based computational model confirmed that the rigidity-dependent durability of microtubule alignment dominates their collective behavior.

MAIN TEXT

Collective motion is a self-coordinated phenomenon that widely exists in nature. The collective motion can be seen at the macroscopic level of fish schools and bird flocks[1,2] to the microscopic level of bacterial colonies,[3] cell cultures,[4] and self-propelled microparticles.[5] Cytoskeleton filaments, such as microtubules (MTs) and actin filaments, play significant roles in regulating cell morphology and resisting environmental mechanical stress.[6,7] In addition, these cytoskeletal filaments self-coordinate to enable essential functions and physiological activities of cells, such as structural support, intracellular transport, motility, and mitosis.[6–8] By interacting with motor proteins, cytoskeletal filaments generate active forces to control the assembly of cellular structures and long-range patterns[9,10] or active nematic.[11,12]

Furthermore, collective motions emerge in the *in vitro* reconstructed gliding system of cytoskeleton filaments, in which MTs or actin filaments are propelled by surface-bound motor proteins (kinesin, dynein, or myosin).[13–16] A number of diverse behaviors and various patterns, such as flocks, polar streams, vortex, and spirals, by different mechanisms have been reported in experimental systems.[16–18] The persistence length (L_p) of filaments was shown to be a critical and apparent factor that determines the orientational flexibility, affects their gliding and alignment behavior, and governs the rheological properties of filament networks.[19–23] The L_p is likely to play a crucial role in the phase transition process during collective motion. Motor-propelled microtubule filaments with shorter L_p are easier to change their gliding direction, indicating softer filaments have larger orientation flexibility than stiffer ones. However, the effect of the orientation flexibility of gliding filaments on collective motion has not been clarified. Although a myriad of theoretical models and hypotheses have been proposed to explain the underlying

mechanism and predict potential patterns in collective motion,[24–31] experimental verifications are still lacking significantly.

Herein, we investigated how the orientation flexibility of self-propelled filaments affects the collective motion, using MTs with predefined L_p gliding on the surface-coated kinesin-1 motors in the presence of a depletant, methylcellulose (MC). We observed distinct patterns formed by MTs with different L_p. To understand the underlying mechanisms behind the formation of different patterns, we analyzed the behaviors of the individual "seed" bundles formed initially. The entire phase transition process during the collective motion of the MT-kinesin system was traced and quantitatively evaluated. Furthermore, binary collisions were statistically analyzed to understand how L_p of MTs influences a change in the orientation angle after collisions. The computational model demonstrated that L_p alone can explain differential patterns formed by MTs. Our study illustrates how the orientational perturbation of self-propelled filaments affects their collective behavior and highlights the role of L_p-dependent durability of alignment played in collective motion.

RESULTS AND DISCUSSION

Different patterns formed by collectively gliding MTs with different L_p. The L_p of MTs is affected by their polymerization conditions, including the types of nucleotides and their growth rate.[32] A faster growth rate of MTs induces more lattice defects and thus softens the MTs.[33,34] Based on this mechanism, a method for controlling L_p of MTs by altering tubulin concentrations has been presented in our previous work.[35] Herein, three types of MTs with different L_p were

engineered using two types of nucleotides (GTP or GMPCPP) and two different growth rates of the MTs (Figure 1a and Supplementary Table S1). The growth rates of the MTs were modified by adjusting the tubulin concentration (*i.e.*, at 30 or 100 μM). L_p of the three groups of MTs, that is, *softer GTP-MTs*, *stiffer GTP-MTs*, and *GMPCPP-MTs*, was 0.65 ± 0.24, 1.93 ± 0.82, and 3.54 ± 0.99 mm, respectively, measured using our previous method.[35]

Three groups of MTs with different L_p were utilized to conduct *in vitro* motility assays on the lawn of highly processive motor proteins kinesin-1 in the presence of 0.3 wt% MC (Figure 1b). A high surface density of the MTs (5.5 ± 0.3 filaments μm^{-2}) was adopted. No substantial difference in the average length (9.6 μm) and gliding velocities of MTs (601 ± 0.04 nm s^{-1}) between the three MT groups (see Supplementary Figure S1) was observed. Initially (0 min, the addition time of adenosine triphosphate, ATP), the MTs were uniformly and randomly distributed in the field in an isotropic state (Figure 1c). Thereafter, the MTs were propelled by kinesin-1 motors to glide and frequently collide with other MTs by consuming ATP. As the orientations of MTs were tuned by the continuous collisions and alignments, collective motion gradually evolved into distinct patterns in the three groups (50 min). Thereafter, *softer GTP-MTs* tended to form a local stream on a large scale, whereas *stiffer GTP-MTs* and GMPCPP-MTs evolved into stable bundles with apparent density waves (Figure 1c).

To characterize differences in patterns formed by the three types of MTs, the length (L_B) and width (W_B) of MT bundles and distance between the bundles (D_B) were measured from the skeletonized images (220 μm × 220 μm) of the MT patterns (Figure 1d). L_B in *stiffer GTP-MTs* (164.3 ± 36.2 μm) and *GMPCPP-MTs* (141.5 ± 72.7 μm) was larger than that in *the softer GTP-MTs* (48.7 ± 39.6 μm). No statistical difference was found between the *stiffer GTP-MTs* and *GMPCPP-MTs* groups. Both W_B and D_B in *stiffer GTP-MTs* ($W_B = 3.8 \pm 2.3$ μm; $D_B = 8.3 \pm 3.8$

µm) were larger than those *of GMPCCP-MTs* ($W_B = 1.5 \pm 0.4$ µm; $D_B = 2.8 \pm 1.8$ µm). This observation indicated that the bundles formed by *stiffer GTP-MTs* and *GMPCCP-MTs* are also different. These results imply that the patterns formed in collective motion are governed by L_p of the filaments. Furthermore, the three types of MTs were classified with an accuracy of 97.7% based on their different features using our previously reported method of deep-learning-based image recognition (see Supplementary Text, Model for classifying images and Supplementary Figure S2).[35] The pattern differences between the three MT groups were visualized using the technique of class activation mapping (see Supplementary Text, Visualization of the classification strategy and Supplementary Figure S3),[36] which correspond well with our observed results.

"Seed" bundles formed by MTs with different L_p behave differently. Owing to the high surface density and random orientations of the MTs, they must collide and interact with their neighbors after the addition of ATP. Several neighboring MTs locally align with each other and form a small-scale cluster, which is defined as a "seed" bundle. The formation of seed bundles is the first and essential step for the transition process and occurrence of collective motion.[37] As the first step to investigate the formation mechanisms of the different patterns in three MT groups, we analyzed the behaviors of the MTs during the first several minutes after adding ATP.

It was found that the seed bundles formed by MTs with different L_p behaved differently (Figure 2a). For the *softer GTP-MT* group, seed bundles emerged and disappeared frequently with random distributions in the field. The single seed bundles can be assembled in approximately 30 s but retained transiently for 42 s (Figure 2a). The seed bundles formed in the *stiffer GTP-MT* group had a relatively long survival time from the formation time of ~139 s and tended to merge with their neighboring seed bundles to develop into a large cluster at ~240 s (Figure 2a). The

behaviors of seed bundles in the *GMPCCP-MT* group were different from those of the two other groups. These *GMPCCP-MTs* seed bundles are persistent with a survival time of extremely longer than 120 s, which was formed at ~151 s and retained till ~271 s (Figure 2a). Once the *GMPCCP-MTs* seed bundles were developed, they took the roots to hold their locations. Their scales remained stable without dilating or being swallowed by the neighbors (Figure 2a). Moreover, the differences in the behaviors of the seed bundles between the three MT groups were amplified to larger length-scale and thus influenced the entire MT motion system (Figure 2b). Compared with disordered gliding orientations of *softer GTP-MTs*, *stiffer GTP-MTs* tended to cluster together, while *GMPCPP-MTs* were well nematically structured (Figure 2c).

These results indicate that for the first several minutes after the addition of ATP, the stabilities of these local seed bundles are markedly different depending on L_p of MTs. That is, soft "seeds" (formed by *softer GTP-MTs*) tend to disintegrate and fail to develop any type of stable structures (Figure 2a,b) that are similar to the transient "seed cluster" formed by actin filaments reported by Suzuki *et al.*.[37] For *softer GTP-MTs*, because of the short survival time of an individual seed bundle, the bundles appeared and disappeared too frequently to interact with other bundles. With the disordered motions of *softer GTP-MTs,* no obvious bundles were observed, and no apparent patterns emerged for the first 5 min (Figure 2b). By contrast, the seed bundles formed by the two other groups are more robust to be long-lived with growing up to a larger community (by *stiffer GTP-MTs*) or holding their position and elongating in the axial direction with an apparent nematic array (by *GMPCPP*-MTs) (Figure 2a,b). As to *stiffer GTP-MTs*, the long survival time of the seed bundles allowed them to recruit neighboring seed bundles and MT filaments. With fewer inside MTs leaving and more nearby bundles and MT filaments joining, *stiffer GTP-MTs* showed an evident tendency to aggregate to each other (Figure 2c), which gradually developed in

a large-scale cluster for the first 5 min (Figure 2b). For *GMPCPP-MTs*, owing to intense collisions between MTs, a large number of identifiable bundles appeared at ~2 min. They were stable and uniformly distributed throughout the field. In contrast to *stiffer GTP-MTs*, the seed bundles of *GMPCPP-MTs* exhibited an obvious bias in elongating their axial length by linking other adjacent MTs rather than broadening their scale in the radial direction. Finally, a nematic array was formed with continuously tuned the orientations of *GMPCPP-MTs* (Figure 2b,c). Although these seed bundles for *stiffer GTP-MT* and *GMPCPP-MT* groups are premature and still far from their final stable state, they exhibited the capability of recruiting other filaments from the surroundings (*stiffer GTP-MTs*) and enhancing the nematic alignment (*GMPCPP-MTs*), respectively (Figure 2c). Neither of the two features is present in *softer GTP-MTs*.

Different phase transition processes in the three MT groups. To investigate the time evolution process from an initial isotropic state to the final nematic patterns, the collective motions of the MTs were tracked over time (Figure 3a, Supplementary Movies S1 to S3). The nematic order parameter (*S*), which was calculated using the orientation angle distribution of MTs, was introduced to quantitatively evaluate the nematic level of the gliding MTs system (Figure 3b).[38] Initially, the value of *S* was defined as 0 since the entire system was assumed to be in an isotropic state with MTs randomly distributed and oriented (0 min, Figure 3a). With MTs continually colliding and aligning with their neighbors; their gliding directions are gradually tuned in a polar or antipolar fashion, and then *S* of the whole system will increase. We found that the three MT groups have different nematic levels that vary over time during the phase transition process. For *softer GTP-MT*s, *S* increased relatively slowly to ~0.24 for the first 10 min. Then, it fluctuated for 20–40 min due to the frequent formation and disintegration of short-lived bundles till a large-scale uniform stream formed at 50 min with the *S* value reaching ~0.54. By contrast, *S*

for *stiffer GTP-MTs* and *GMPCPP-MTs* changed significantly faster initially after adding ATP. Their S increased to ~0.33 and ~0.67 after 5 min, respectively, and reached their inflection points of ~0.60 at ~20 min and ~0.70 at 10 min, respectively (Figure 3b). Thereafter, the variations in S for *stiffer GTP-MTs* and *GMPCPP-MTs* were small and eventually the values of S were stabilized at approximately 0.62 and 0.80, respectively (Figure 3b). Overall, the emergence time of an identifiable ordered structure was ~50, 20, and 10 min for *softer GTP-MTs*, *stiffer GTP-MTs,* and *GMPCPP-MTs*, respectively, which suggests that the speed of the phase transition was positively correlated with L_p of MTs.

Additionally, skewness (*Sk*) was introduced to quantify the bundling level in collectively gliding MT systems.[38] At the start time (0 min), MTs were assumed to be in a homogeneous state, where the fluorescent intensities of the MT filaments were assumed to exhibit a normal distribution (*Sk* = 0). When bundles with brighter belt-like patterns emerged, pixel values of the corresponding areas increased, and the distribution of fluorescence intensity in the field was skewed. Generally, a larger value of *Sk* suggests a higher bundling level. Because of the large number of seed bundles formed in the beginning, the value of *Sk* in the three groups increased sharply from 0 to ~1.3 for the first 3 min (Figure 3c). After that, the *Sk* of *softer GTP-MTs* did not rise and fluctuated with the emergence and disappearance of transient bundles. *Sk* of *Stiffer GTP-MTs* and *GMPCPP-MTs* showed a similar variation for the first 10 min. *Sk* for *stiffer GTP-MT*s continued to increase as more seed bundles merged to form a large dense bundle. For *GMPCPP-MTs*, with the formation and growth process of seed bundles, *Sk* continued to rise from the beginning and reached its peak point of ~1.8 at 10 min. Both S and *Sk* simultaneously reached their maxima (at 10 min), suggesting that the *GMPCPP-MT* system entered a nematic state at 10 min.

Subsequently, the scale and structure of bundles formed by *GMPCPP-MTs* remained constant with *Sk* maintaining a relatively stable value of ~1.8 (Figure 3c).

The formation of different patterns in the three MT groups originated from their distinct phase transition processes. The dynamics of phase transitions were previously reported to be a function of filament density, where fewer filaments take a longer time to form clusters.[37,39] Once MT density becomes higher than a specific value, collective motion emerges with a consistent level of the nematic order.[15,40] Here, the phase transition processes of MTs were observed to vary with respect to their L_p while maintaining their surface density constant. The MTs with longer L_p transform faster from the original isotropic phase to enter the nematic state (Figure 3a,b). Additionally, compared to *softer GTP-MTs* that were disturbed through rounds of turbulences between 20 min and 40 min, *S* in the two other MT groups maintained a smooth transition process and a steady value after 20 min (Figure 3a,b). This can be explained by the fact that differences in the stability of the local seed bundles in the three groups were inherited and amplified to the global scale of the collective motion (Figure 2). In comparison to dispersedly gliding *softer GTP-MTs* and transient bundles formed by them, the bundles formed by stiffer MTs considerably improved the snuggling probability of their neighboring filaments. This enhanced the nematic alignment and accelerated the phase transition.[34] Furthermore, these differences in the phase transition process eventually result in the formation of different patterns, such as local streams, large-scale bundles, and highly nematically organized arrays. These results show that L_p is a significant factor for determining the dynamics of phase transition and pattern formation in collective motion.

This finding is supported by previous literature and can be used to explain differences between previous studies. For instance, Inoue *et al.*[15] reported a local stream similar to the case of *softer*

GTP-MTs, whereas Farhadi *et al.*[39] reported a large-scale bundle similar to that formed by *stiffer GTP-MTs*. Both research groups conducted MT gliding assays using the same type of kinesin-1 with 560 amino acids in length, identical MC concentration (0.3 wt%), and MT concentration (5 µM). However, the polymerization conditions of MTs were different (tubulin concentration of 55.6 µM by Inoue *et al.*,[15] and 45 µM by Farhadi *et al.*[39]). Although L_p of MTs in the two groups was not reported, based on the theory showing that a faster growth rate induced by a higher tubulin concentration softens MTs,[33–35] MTs used in Inoue *et al.* should be softer than that used in Farhadi *et al.* Different L_p of MTs is probably the reason for the formation of different patterns in the two studies.

Durability of the aligned MTs enhanced with longer L_p. The collective motion of MTs evolved with their gliding orientations varied and aligned through continuous interactions and collisions. Because of the high density of MTs in the collective motion, it was difficult to directly visualize the behavior of individual MTs. To understand how L_p of the gliding MTs influences their orientation changes and alignment behaviors during collisions, we examined the behaviors of isolated MTs in a binary collision with a low MT surface density (0.022 ± 0.001 filaments μm^{-2}). Using the same setup as the collective motion assays, the three MT groups (*softer GTP-MTs*, *stiffer GTP-MTs*, and *GMPCPP-MTs*) were used to conduct binary collision assays under four different concentrations of MC (0, 0.2, 0.3, and 0.4 wt%).

First, we analyzed how collisions altered the orientation angle of gliding MTs. According to a relationship between the incoming angle before the collision, θ_{in}, and the outgoing angle after the collision, θ_{out}, the effect of a collision on MT gliding orientation was classified into three classes: (i) polar: $\theta_{in} > \theta_{out}$, (ii) anti-polar: $\theta_{in} < \theta_{out}$, and (iii) non-effect: $\theta_{in} = \theta_{out}$ (Figure 4a). As the binary-collision statistics on θ_{in} and θ_{out} are shown in Figure 4b (see Supplementary Figure S4a

for details), the upper-left ($\theta_{in} < \theta_{out}$) and lower-right areas ($\theta_{in} > \theta_{out}$) represent the anti-polar and polar classes, respectively. We found that the probability of polar increases as the θ_{in} decreases (Figure 4c), whereas the probability of anti-polar increases with θ_{in} increases (Figure 4d). Regardless of L_p and MC concentrations, MTs with an acute θ_{in} ($< 90°$) have an obvious polar bias after collision with a polar probability greater than 50% (Figure 4c and Supplementary Figure S4b). By contrast, MTs with highly obtuse θ_{in} ($> 150°$) tend to be anti-polar with a probability greater than 75% (Figure 4d and Supplementary Figure S4c). Furthermore, we calculated the dispersion level, η_d, from the distances of scattered points far from the diagonal line to quantify the changes in MT gliding orientation caused by a collision (Figure 4e and Supplementary Table S2). No significant differences in η_d ($16.3° \pm 5.4°$) were observed between the 12 conditions (two-way ANOVA, $p > 0.05$), indicating that changes in MT orientation angle after collisions are independent of L_p and MC concentration. The probabilities for being "polar" and "anti-polar" were approximately 50%, whereas few cases of "non-effect" occurred with a negligible probability of ~2% (Figure 4f and Supplementary Table S3). For the "polar" and "anti-polar" cases, no significant differences were observed in the changes of orientation angles ($\theta_{in} - \theta_{out}$) after collisions among the 12 conditions (two-way ANOVA, $p > 0.05$, see Supplementary Figure S4d).

We then studied the change in the orientational correlation of two MTs after the collision. According to the morphologies of the two MTs after a binary collision, all the cases were categorized into three types: (i) crossover, where two MTs collided and crossed by without alignment; (ii) parallel alignment, where two MTs collided and aligned with each other in one direction ($\theta_{out} = 0°$); and (iii) anti-parallel alignment, where two MTs collided and anti-polar aligned with each other in opposite directions ($\theta_{out} = 180°$) (Figure 5a, Supplementary Movies S4

to S6). On collisions in the 12 groups, crossover occurred overwhelmingly (~70%), whereas parallel or anti-parallel alignments took place at ~15% probability (Figure 5b and Supplementary Table S4). Regardless of L_p of MTs and the concentration of MC, the average incoming angle θ_{in} in the polar, non-polar, and non-effect classes was approximately 30°, 90°, and 150°, respectively (Figure 5c and Supplementary Table S5). This indicates that the incoming angle determines whether the MTs will crossover or align.

Lastly, we examined whether L_p of MTs or MC concentration influenced the duration and stability of the aligned MT bundles. The durability of alignment can be characterized by the coupling time indicating how long the gliding tips of two aligned MTs correlate with each other and persist in the same direction. The coupling time is defined by the duration between the collision moment (t_0) and the timepoint when the tip of one MT deviates from the other (t_1) (Figure 6a). The coupling time of aligned MT bundles increased with larger L_p of MTs and higher MC concentration (Figure 6b and Supplementary Table S6), indicating that both orientational persistence and MC-induced depletion forces significantly affect the ability of aligned MTs to maintain their bundling state (two-way ANOVA, $p < 0.0001$). Because the thermal fluctuation of the tips of gliding MTs is inversely proportional to L_p and suppressed by the depletion force originating from MC,[15] stiffer MTs with larger depletion forces have stronger alignment durability.

Based on visualization of behaviors of individual MTs during the collision, we found that the gliding direction altered by the binary collision is independent of L_p of the MTs and the MC-induced depletion force (Figure 4b,e and f). It is noteworthy that whether MTs will be "polar" or "anti-polar" after a collision (Figure 4c,d) and the probability of MT alignment (Figure 5b,c) depend only on the incoming angle θ_{in}, and not on L_p or MC concentration. However, once the

MTs are aligned into bundles, L_p and MC concentration define the durability of the alignment and the orientational correlation as discussed earlier. These results suggest that MTs with different L_p have the same probability of being aligned and forming seed bundles. However, the stability and duration of these bundles are significantly different. This is consistent with our experimental observations that the tendency of the three groups to form bundles is identical from the initial state. It is shown by *Sk* of the three MT groups that share the same variation tendency for the first 3 min (Figure 2c and 3c) but gradually show divergence due to the different stabilities of these formed bundles (Figure 2). Seed bundles are formed by the alignment of MTs with a longer duration time, allowing them to recruit more filaments (as *stiffer GTP-MTs*) or enhance the alignment capability (as *GMPCPP-MTs*) (Figure 2b,c).[31,37] Therefore, differences in the coordinated behaviors between the three MT groups resulted from their different durability of aligned bundles rather than the probability of alignment.

The emergence of the collective motion in the MT-kinesin system was previously proposed to result from the depletion forces induced by MC, which reduces the crossover chance of filaments and promotes their alignment probability from 18% to 62%.[15,40,41] In the absence of depletants, the collective motion failed to emerge in the MT-kinesin system. Herein, we identified a different evolution mechanism of the collective motion in the MT-kinesin system, in which the MC-induced depletion force enhances the endurance of aligned MTs (Figure 6) instead of promoting MT alignment (Figure 5).[42] The alignment probabilities of the MTs in the three groups with the emergence of collective motion are constant at ~30%, indicating that the generation of collective motion in a MT-kinesin system does not solely rely on a high alignment probability. Moreover, the orientation persistence of filaments and the stability of their alignment also play a crucial role. These findings further raise an intriguing point that by increasing L_p of

MTs or enhancing the durability of aligned MTs, such as via microtubule-associated proteins or crosslinkers, the collective motion can also emerge in a MT-kinesin system in the absence of depletants. A previous study demonstrated the feasibility of this proposed scheme. The collective motion emerged with a relatively low snuggling probability of MTs of 36% using 0.25 μM MAP4 fragment in a depletant-absent MT-kinesin system,[15] which is similar to ~30% of our system. The generation mechanism of collective motion can be explained by the fact that MAP4-regulated the surface charges of MTs enhance the stability of the formed MT bundles rather than increasing their snuggling probability during collisions.[15,43]

The stability and durability of aligned MTs depend on their path persistence length, which characterizes the distance of individual MT gilding without reorientation and is determined by the thermal fluctuation of MT leading tip.[44] Theoretically, the path persistence length of gliding MTs is equal to their L_p by assuming that the motor proteins bound with MTs like a fixed and inextensible "anchor".[45] However, the reported values of path persistence length of MTs are one order of magnitude smaller than their L_p.[20,21,46] This discrepancy can be explained by that the length of the MT leading tip can extend much longer than the theoretically predicted value.[47] In addition to L_p and depletion force, other factors involved in determining the extended length of MT leading tip, including the density, tail length, type, and landing rate of motors, influence the fluctuation amplitude of MT leading tips and define their gliding trajectory.[48–50] Moreover, several factors such as gliding velocity, conformation change, detachment rate of MTs; substrate roughness; and temperature affect the alignment of MTs during collisions.[51,52] Given that the depletion force (0.11 pN by 0.3 wt% MC) induced by MC[15,53] is even lower than the stall force (5–7 pN) generated by a single kinesin molecule,[54,55] it is unclear how much the depletion force

contributed to promoting the alignment of kinesin-driven MTs, which needs further investigations.

Computational model validates L_p-dependent MT pattern formation. The experimental results suggest that the phase transition and pattern formation emerging during the collective motion of MTs are mainly affected by the L_p-dependent durability of MT alignment. This conclusion was validated using an agent-based computational model of MTs with two different L_p (0.63 and 1.93 mm) which correspond to those of *softer GTP-MTs* and *stiffer GTP-MTs*. Softer MTs failed to develop any stable structure in the simulation (Figure 7a), whereas stiffer MTs formed stable bundles that grow in size over time (Figure 7b), which matches the experimental results.

The bundles formed in the two MT groups were quantitatively characterized by their bundle size, formation time, and disintegration time. We considered a structure consisting of more than 20 MT filaments ($N_B \geq 20$) to be a bundle, where N_B indicates bundle size. The "formation time" of a bundle whose size is N_B is defined as the time required for the number of MT filaments to increase from $N_B/2$ to N_B. The "disintegration time" is defined as the time required for the bundle to lose half of the filaments with the bundle size decreasing from N_B to $N_B/2$. We first compared the size of bundles in the two groups at 1000 s, 1500 s, and 2000 s after the simulation began (Figure 7c). At 1000 s, there was no significant difference in bundle size between softer and stiffer MTs (two-tailed Mann-Whitney-Wilcoxon test, $p > 0.05$). However, a difference in the bundle size between the two groups gradually increased over time, and a significant difference was observed at 1500 s ($p < 0.05$) and 2000 s ($p < 0.001$) (Figure 7c). Softer MTs failed to develop a thick bundle, whereas bundles formed by stiffer MTs tended to merge and grow into a

larger-scale structure. As indicated by the size of several individual bundles over time (Figure 7d), bundles in the softer MT group had smaller bundle size ($N_B < 45$) and disintegrated quickly with a short survival time (< 20 s), whereas bundles in stiffer MT group had larger size ($N_B > 130$) and could be maintained for > 200 s (Figure 7d). To investigate reasons for the differences in the size and survival time of bundles between the two groups, we compared the formation and disintegration time of bundles. The formation and disintegration time of each bundle were normalized by its bundle size N_B to account for the impact of bundle size on them. Bundles in both softer and stiffer MTs had similar formation time ($p > 0.05$), but disintegration time was significantly different ($p < 0.05$) (Figure 7e). It can be explained that stiffer MTs with higher orientational persistence had a weaker disintegration tendency than softer MTs. With a longer disintegration time, stiffer MTs may survive longer and recruit more filaments to further develop a dense bundle. The results indicate that what determines the bundle formation is alignment durability or disintegration propensity, not the bundle formation capability.

Inspired by the classic Vicsek model,[24] "alignment" and "noise" have been two basic components to determine the phase transition of collective motile agents, including self-propelled particles,[25] hard rods,[26,27] and filamentous active matters.[28–31] As a parameter defining the persistence distance of a motile agent, the L_p has been widely recognized to be inversely proportional to noise.[56–58] Although several theoretical models investigated the influence of L_p on collective motion, experimental validations are still limited significantly. Here, we systematically investigated the influence of L_p-dependent orientational noise of MTs on their collective motion. Our results corroborate the previous theoretical studies that a longer L_p with smaller noise variance can promote collective behavior and enhance phase order. Stiffer MTs have a faster phase transition rate and higher order level than the softer ones. On the other side, our results

suggest that the duration of alignment, rather than alignment probability, impacts the evolution process of collective motion. The current existing theoretical models are incapable to describe the findings. A link between the "orientational noise" and "alignment durability" was established, which should be considered in future theoretical models.

In addition to the collective behaviors and phase dynamics, the rheological properties of the filament network should be influenced by their L_p. The elastic plateau modulus of semiflexible biopolymer networks, including DNA tubes, actin filaments, and cardiac thin filaments, was reported to be dependent on their L_p.[22,23] As solid rod-like filaments, MTs have significantly longer L_p than these semi-flexible filaments. Due to the difficulty of tuning the stiffness of biopolymers, the relationship between the L_p of a single MT and the rheological properties of their filament network is unclear. Our work provides a suitable experimental platform, which can be readily extended for studying the influence of filament rigidity on the viscoelastic properties of the polymer network.

CONCLUSIONS

The influence of the L_p of MTs on their collective motion was investigated using an *in vitro* reconstructed system of MTs and kinesin-1 in the presence of MC. In accordance with the experimental observations, the simulation results show that stiffer MTs formed more durable bundles with a larger size, whereas softer bundles fail to maintain stable bundles due to the frequent formation and disintegration of aligned filaments. Different collective behaviors and patterns formation are solely determined by L_p of MTs in the simulations, which further demonstrates that L_p-dependent durability of aligned MTs determines the phase transition and

pattern formation in collective motion. The knowledge presented here can be generalized for a better understanding of active matter. Moreover, our study constructs a quantitative experimental scheme to study and examine orientational noise-dependent collective behaviors in the future.

METHODS

Protein preparation. Tubulin proteins were purified from porcine brains and then fluorescently labeled with succinimidyl ester-conjugated tetramethylrhodamine (TAMRA) (C-1171; Invitrogen, USA).[59] The hexahistidine (His6)-tagged kinesin-1 proteins (1–465aa) were purified from *Escherichia coli* using nickel-nitrilotriacetic acid affinity resin.[60]

Three MT groups (*softer GTP-MTs*, *stiffer GTP-MTs*, and *GMPCPP-MTs*) with different L_p were polymerized under different conditions (Supplementary Table S1). All MTs were polymerized from TAMRA-labelled tubulin at 37°C for 30 min and then stabilized with 20 μM paclitaxel after elongation. L_p of MTs was measured with our previous method.[35] The measured MTs were partially immobilized on a gold stripe via biotin–streptavidin binding. The left part of MTs freely fluctuated under the thermal energy as a cantilever beam tethered at one end, which was set as the origin of an orthogonal coordinate system. The shape of the fluctuating segment $y(s)$ was parameterized by the following equations:

$$y(s) = \sum_{n=1}^{\infty} \sqrt{\frac{1}{L}} a_n W_n\left(\frac{s}{L}\right) \tag{1}$$

and

$$W_n\left(\frac{s}{L}\right) = \frac{-\cosh(q_n) - \cos(q_n)}{\sin(q_n) + \sinh(q_n)}\left(\sin\left(\frac{q_n s}{L}\right) - \sinh\left(\frac{q_n s}{L}\right)\right) \tag{2}$$

$$+ \cos\left(\frac{q_n s}{L}\right) - \cosh\left(\frac{q_n s}{L}\right)$$

where s is the path length from the immobilized end along the MT, L is the MT length, q_n is 1.875 ($n = 1$), 4.695 ($n = 2$), 7.855 ($n = 3$), and ($n - 0.5$) π ($n \geq 4$).[61] The thermal energy was assumed to be equated with the bending energy of MTs. The L_p of MTs was derived from the variance of amplitude in each nth mode, $var(a_n)$.

$$L_p = \frac{1}{var(a_n)}\left(\frac{L}{q_n}\right)^4 \tag{3}$$

Motility assay. The glass substrates (C218181 and C024361; Matsunami Glass, Osaka, Japan) used for motility gliding assays were treated with a piranha solution at 60°C for 10 min, rinsed with deionized water, and dried using nitrogen gas. The central area (5 × 5 mm) of the glass substrate was exposed to air plasma for 40 s at a flow rate of 50 sccm with the surrounding area covered by tape.

Following three types of Piperazine-N, N'-bis(2-ethanesulfonic acid) (PIPES)-based buffer solutions were used in the assay: (i) BRB80, which contains 80 mM PIPES, 1 mM EGTA, and 1 mM MgCl$_2$ with a pH of 6.8; (ii) casein buffer, which contains 0.3 mg ml^{-1} casein dissolved in BRB80 and (iii) motility buffer, which contains BRB80 added with 5 mM ATP, 0–0.4 wt% MC, 20 mM paclitaxel, and O$_2$ scavenger (36 mg ml^{-1} catalase, 216 mg ml^{-1} glucose oxidase, and 25 mM D-glucose).

Gliding assays were conducted through the introduction of MTs onto kinesin molecules with motility buffer. First, 2 mg ml^{-1} streptavidin (434301, Thermo Fisher Scientific) was introduced and non-specifically bound to the glass substrate. The chamber was washed with BRB80 solution, and then biotin-conjugated kinesin-1 (0.154 mg ml^{-1}) was added and incubated for 5

min and immobilized on the glass via biotin-avidin binding. After washing with casein buffer, 25 µM MTs and motility buffer were added. All assays were performed at 25°C.

Image acquisition. Images were acquired using an IX73 inverted epifluorescence microscope (Olympus, Tokyo, Japan) with an excitation filter (GFP/DsRed-A-OMF, Opto-Line International, Inc.) and 60 × oil-immersion objective. The exposure time was set to 50 ms with a frame rate of 1 frame s^{-1} and a recording period of 300 s. The addition time of the motility buffer was set to 0 min, and the entire observation period for each assay was ~ 60 min, at which MTs slow down gradually and stop gliding eventually with ATP molecules used up. Captured images were stored as sequential image files in TIFF format using the HCImage software (Hamamatsu Photonics).

Data analysis. The nematic order parameter (S) was defined as:

$$S = \frac{1}{N} \sqrt{\left(\sum_{i=0}^{180} f_i \cdot cos2\theta_i\right)^2 + \left(\sum_{i=0}^{180} f_i \cdot sin2\theta_i\right)^2} \qquad (4)$$

where N is the total pixel number of all the MTs in the image, θ_i (i = 0–180) is the orientation angle with a discrete value of i degrees, and f_i indicates the frequency of MTs orientated at θ_i.[15] It was calculated with the plugin of Directionality[62] in ImageJ (National Institutes of Health).

The skewness (Sk) was defined as:

$$Sk = \frac{1}{N} \sum_{i=1}^{n} \left(\frac{I_n - \bar{I}}{\sigma}\right)^3 \qquad (5)$$

$$\sigma = \frac{1}{N} \sum_{i=1}^{n} (I_n - \bar{I})^2 \qquad (6)$$

where N is the total pixel number of all the MTs in the image; I_n is the pixel intensity of each MT; $\bar{I}$ is the mean intensity of MT pixels.[38]

The original fluorescent images of MTs were denoised with a band-pass filter and then binarized using the ImageJ software. The widths of the MT bundles and inter-bundle distances were measured from the binarized images (Supplementary Figure S5).[63] The lengths of the MT bundles were measured with an ImageJ plugin—Analyze Skeleton.[64] Multiple significance tests were conducted using Steel-Dwass tests at a critical value of $p < 0.05$.

In the low-density binary collision assays, the MT density was directly measured from the obtained images using ImageJ. For the high-density collective motion assays, the MT density was evaluated using a dilution scheme for the fluorescent MTs. Firstly, an alternative MT solution with the same MT concentration (25 µM, as used in the collective motion assays) was prepared by mixing TAMRA-labelled and non-labeled MTs (labeled : unlabeled ratio was 1 : 500). Thereafter, an alternative solution was used to conduct the collective motion assay, as described above. The surface density of the TAMRA-labeled MTs was directly measured using ImageJ. The actual MT density was estimated from the density of TAMRA-labeled MTs and the ratio of labeled: non-labeled MTs.

To obtain the velocity vector fields, two sequential frames captured with an interval of 6 s were used to conduct the PIV analysis. The distances of all the particles that moved between the two frames were calculated based on the principle of the least squares. The real displacements of the particles during the interval of 6 s between the two frames were predicted by repeating this

analysis with an interrogation window (32 × 32 pixels) for each image. All processes were performed using the OpenPIV Python package.[65]

To measure the orientation angles of the gliding MTs during binary collisions, the leading tips of the gliding MTs were tracked using Mark2 image analysis software at 1 s intervals. The incoming and outgoing angles of the two colliding MTs were calculated from the differences between their orientation angles. A two-way ANOVA analysis was conducted to evaluate the statistical significance.

Agent-based model. We developed an agent-based model built based on Brownian dynamics with the Langevin equation to mimic the motility assay (see Supplementary Text, Brownian dynamics and Supplementary Table S7). In this model, MT filaments were simplified into serially connected cylindrical segments with polarity defined by plus and minus ends. The displacements of MTs at each time step are calculated by the Langevin equation. For deterministic forces in the Langevin equation, we consider extensional and bending forces as well as a repulsive force acting between overlapping MT filaments. In addition, the deterministic forces include a propelling force oriented toward the pointed end that mimics a force exerted on MTs by kinesin motors fixed on a surface (see Supplementary Text, Propelling force and Supplementary Figure S6a). To simulate the motility assay, a two-dimensional simulation domain (100 × 100 μm) is employed. In the domain, MTs are nucleated by allocating one MT segment with random positions and random orientations. Then, for polymerization, each MT is elongated by the addition of segments. By varying the nucleation rate, $k_{n,MT}$, with the constant polymerization rate, $k_{+,MT}$, the average length of MTs is set to a specific value to match experimental conditions. In each simulation, we quantify the dynamics of bundle formation and disintegration by keeping track of the number of MTs belonging to each bundle and by

calculating the formation time and disintegration time of a bundle (see Supplementary Text, Quantification of bundle dynamics in simulation and Supplementary Figure S6b).
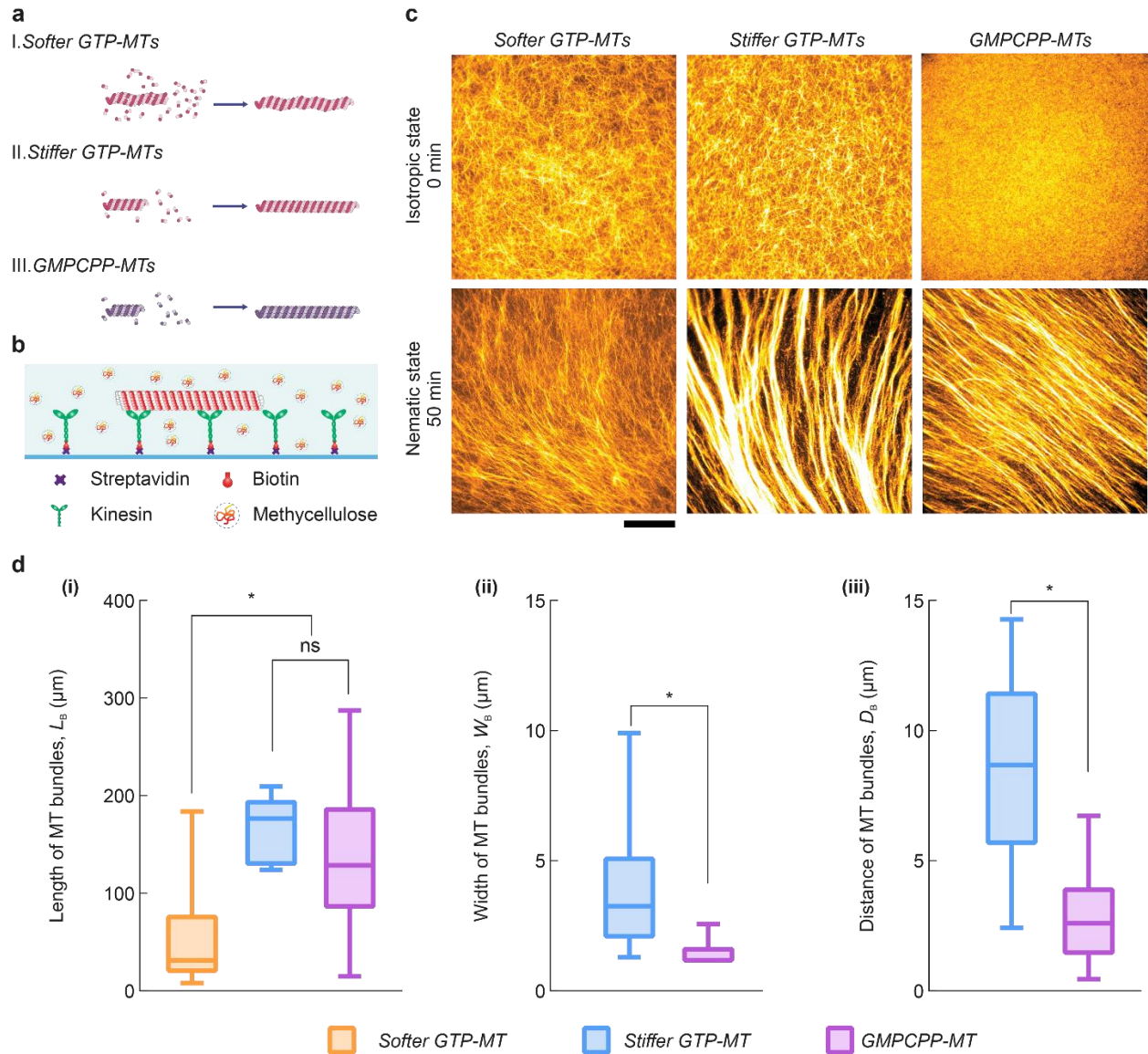
Figure 1. Distinct patterns formed by collectively gliding MTs with different persistence length (L_p) in *in vitro* motility assays. (a) MTs with various L_p were prepared by modifying their growth rate via changing the tubulin concentration in the presence of GTP or GMPCPP, and named as *softer GTP-MTs*, *stiffer GTP-MTs,* and *GMPCPP-MTs*, respectively. (b) MT gliding assays were conducted within a reconstructed MT-kinesin system in the presence of methylcellulose (MC). (c) From the initial isotropic state, three groups of MTs with different L_p formed distinctive pattens at the nematic phase. The addition time of ATP was set as 0 min. MT surface density, $\rho_{MT} \approx 5.5$ filaments μm^{-2}. Scale bar = 50 μm. (d) Characteristics of the bundles formed by the MTs with different L_p. Box plot with the whiskers extended to cover the maximum and minimum values of measurement data. The main box covers the upper to lower quartiles while the median value is represented by the horizontal line. Steel-Dwass test was conducted (ns : $p > 0.05$; *: $p < 0.05$) for (i) length of a bundle, L_B (N =156 for *softer GTP-MTs*; N = 53 for *stiffer GTP-MTs* and N = 34 for *GMPCPP-MTs*) (ii) width of a bundle, W_B (N = 18 for *Stiffer GTP-MTs* and N = 13

25

for *GMPCPP-MTs*); and (iii) distance, D_B between the bundles ($N = 17$ for *Stiffer GTP-MTs* and $N = 12$ for *GMPCPP-MTs*).

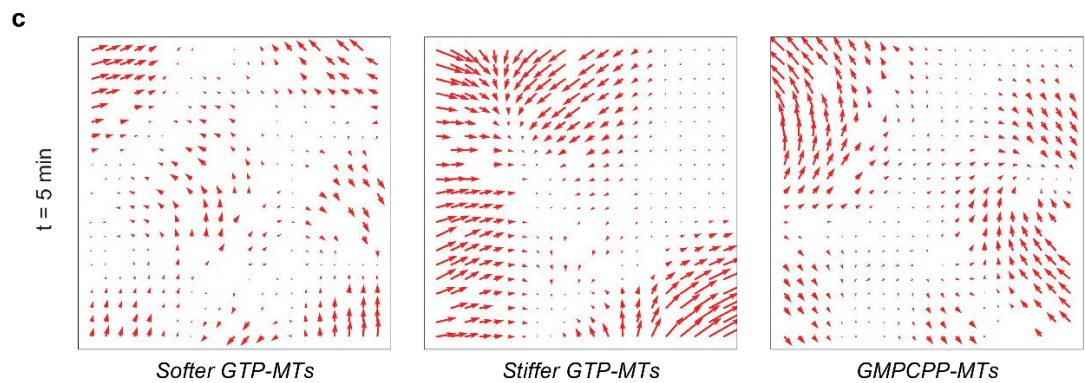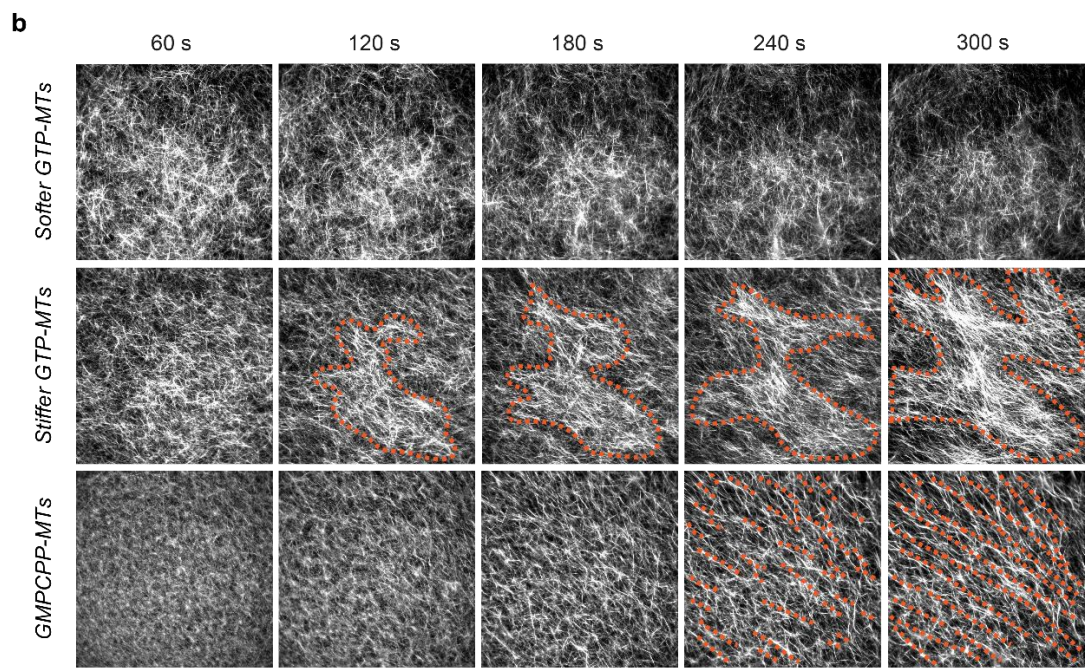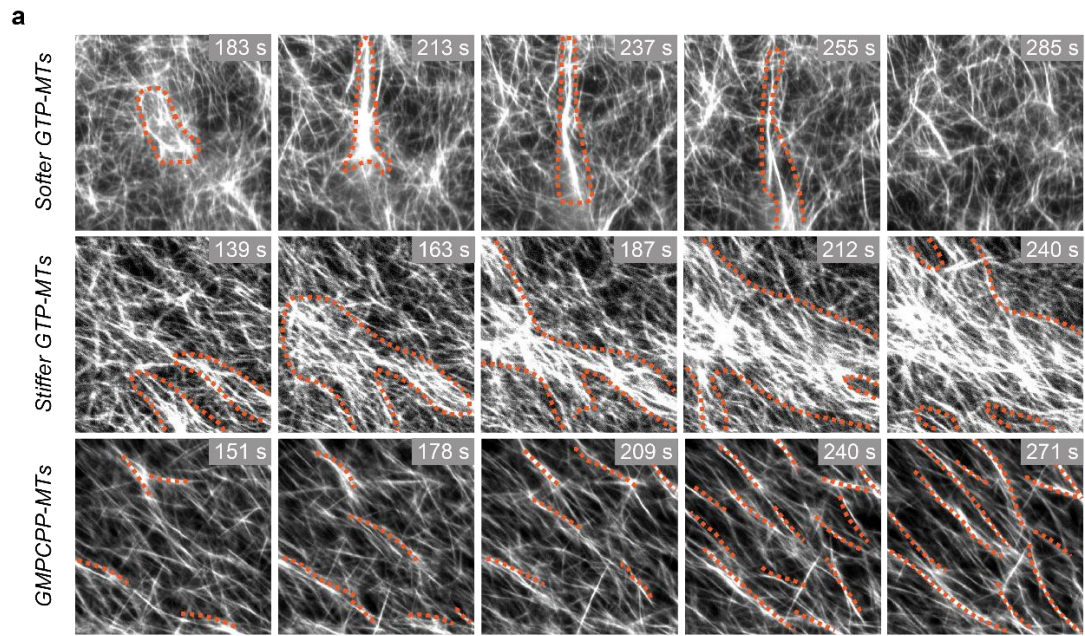**a**

b

c

27

Figure 2. Seed bundles behave differently according to the L_p of MTs. (a) Several locally nearby MTs tend to align with each other and form small-scale clusters, which are defined as "seed" bundles. Distinct behaviors of the seed bundles formed by MTs with different L_p are observed during the first 5 min after adding ATP. Seed bundles in the *Softer GTP-MT* group were assembled between ~183 s and ~213 s but retained transiently between ~213 s and ~255 s; while the *Stiffer GTP-MTs* seed bundles have a relatively long survival time and merge with their neighbors to develop into a large cluster. The seed bundles formed by *GMPCCP-MTs* are persistent with an extremely long survival time. They appear to take root holding their locations and turn their orientation nematically. The addition time of ATP was set as 0 s. MT surface density, $\rho_{MT} \approx 5.5$ filaments μm^{-2}. Scale bar = 5 μm. (b) Time track the seed bundles of the three groups during the first 5 mins after adding ATP. The performance differences of the three types of seed bundles have emerged locally from the beginning and then been inherited and self-amplified to a global scale. MT surface density, $\rho_{MT} \approx 5.5$ filaments μm^{-2}. Scale bar = 50 μm. (c) Velocity vector field of the MTs in the three groups with a lag time of 6 s at 5 min after adding ATP generated via particle image velocimetry (PIV) analysis.
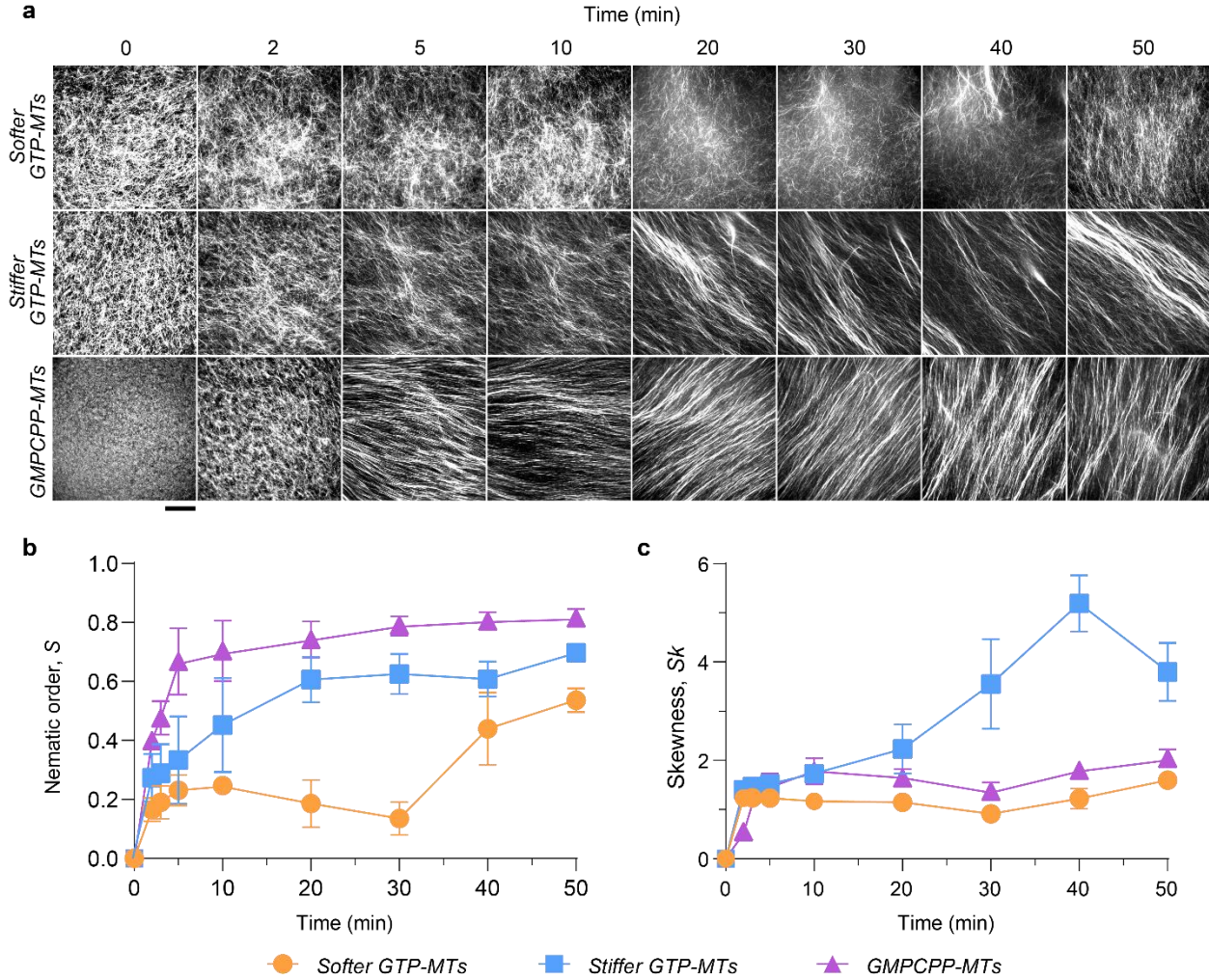
Figure 3. Phase transition and dynamics are influenced by the L_p of MTs. (a) Performance differences in the three types of MTs have existed from the beginning of the whole transition process till distinct polar patterns are formed with stable nematic structures. The addition time of ATP was set as 0 min. MT surface density, $\rho_{MT} \approx 5.5$ filaments μm^{-2}. Scale bar = 50 μm. (b) Nematic order parameter, S is used to monitor the nematic level of the collectively gliding MTs. Data points were sampled at 0, 2, 3, 5, 10, 20, 30, 40, and 50 min. A two-way ANONA analysis was conducted, and a sig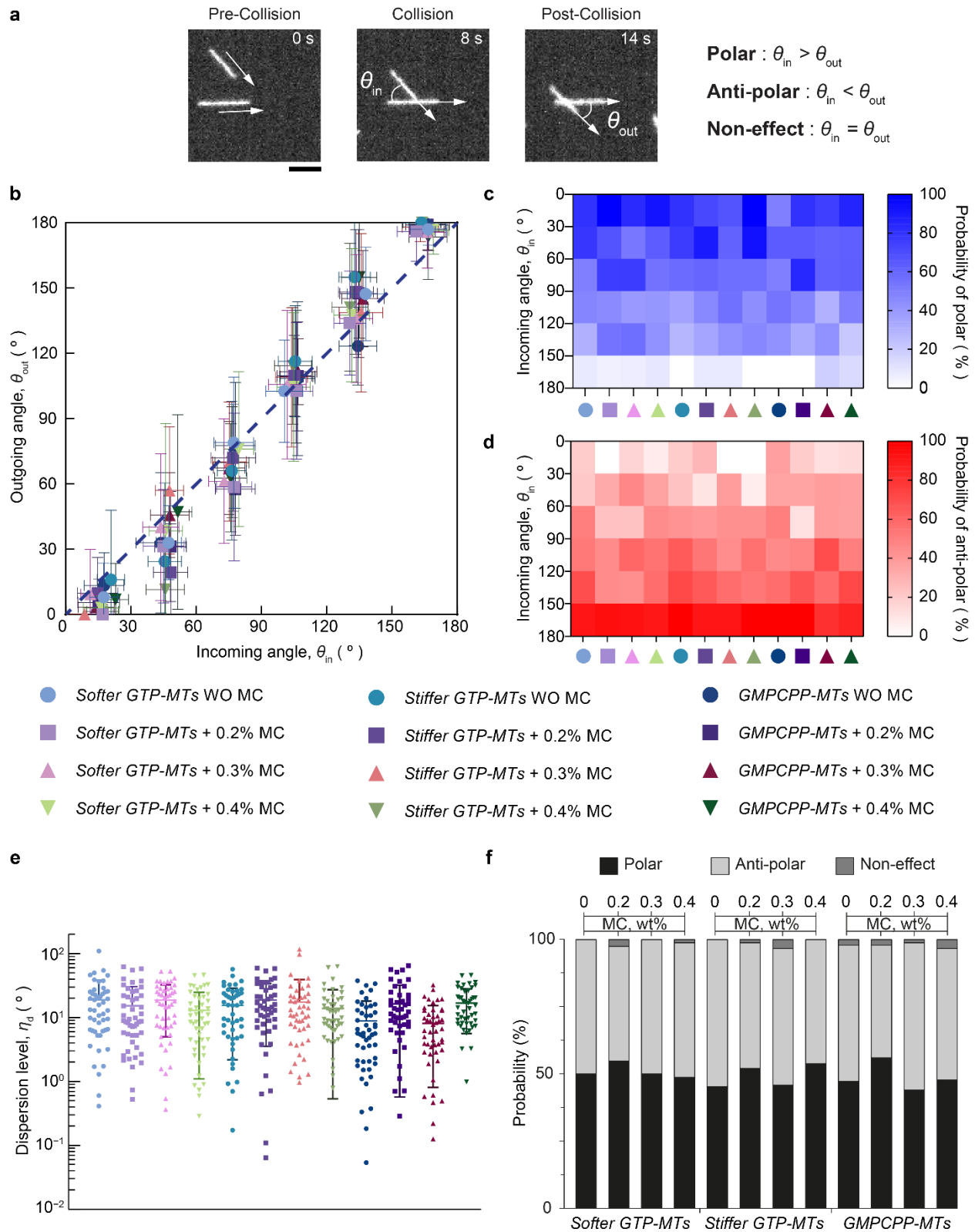nificant difference was detected ($N = 9$, $p < 0.005$). (c) A parameter of skewness, Sk indicates the bundling level of the collectively gliding MTs. Data points were sampled at 0, 2, 3, 5, 10, 20, 30, 40, and 50 min. A two-way ANONA analysis was conducted, and a significant difference was detected ($N = 9$, $p < 0.005$).

Figure 4. Gliding angles of the MTs changed by the binary collision are independent of L_p. (a) Effects of the binary collisions on the MT orientation angle are defined according to the

relationship between the incoming angle, θ_{in} and outgoing angle, θ_{out}, polar ($\theta_{in} > \theta_{out}$), anti-polar ($\theta_{in} < \theta_{out}$) and non-effect ($\theta_{in} = \theta_{out}$). MT surface density, $\rho_{MT} \approx 0.022$ filaments μm^{-2}. Scale bar, 5 μm. (b) Distribution of θ_{in} and θ_{out} (plotted with binning of 30º, error bar plotted with standard deviation) in the three MT groups with different concentrations of MC. The blue-dashed line ($\theta_{in} = \theta_{out}$) represents no change in the MT orientation angle after the collision. (c) Probability of polar cases occurred under different θ_{in}. The θ_{in} in the heatmap was plotted with a binning of 30º. (d) Probability of anti-polar under different θ_{in}. (e) A parameter of dispersion level, η_d, calculated from the distances of the scattered points far from the diagonal line is introduced to quantify the effects of collisions on the MT gliding orientation. Data plotted with the same colors and symbols as (b), (c), and (d). Error bar plotted with SD, and two-way ANONA analysis was conducted. No significant difference was detected ($N = 1200$, $p > 0.05$). (f) Probability of the three different effects of binary collision MTs orientation (polar, anti-polar, and non-effect). The probabilities of "polar" and "antipolar" were roughly equal to ~50%, while few cases of "non-effect" occurred with a negligible probability of ~2%. A two-way ANOVA analysis was conducted, and no significant difference was detected ($N = 1200$, $p > 0.05$).
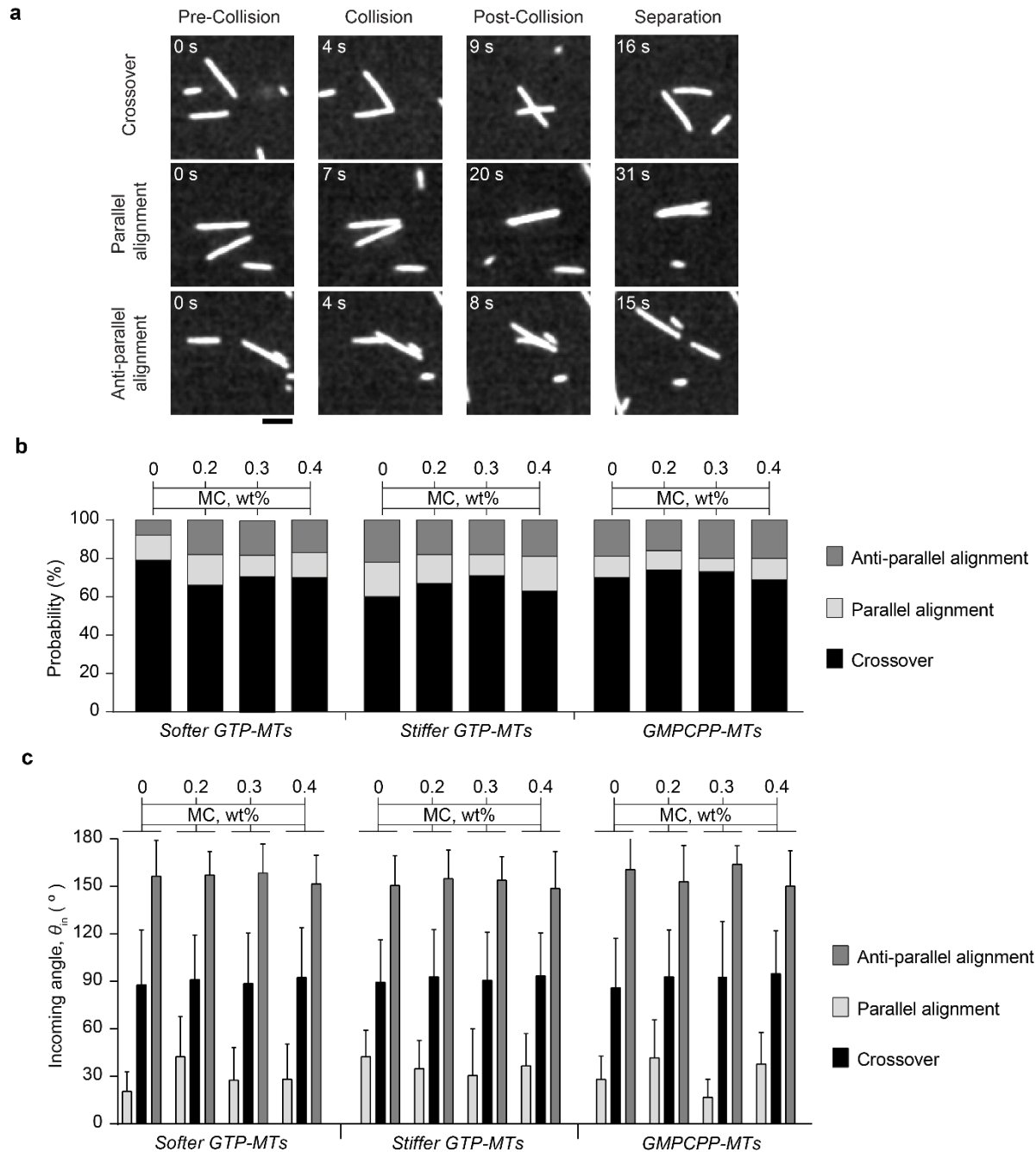
Figure 5. Probabilities of crossover and alignment of two colliding MTs are only determined by θ_{in}. (a) Three different collision results are defined as crossover ($\theta_{out} \neq 0°$ and $180°$), parallel alignment ($\theta_{out} = 0°$), and anti-parallel alignment ($\theta_{out} = 180°$). Scale bar, 5μm. (b) Probability of the three results of binary collision (crossover, parallel alignment, and anti-parallel alignment) in the three MT groups with different concentrations of MC. A two-way ANONA analysis was conducted, and no significant difference was detected ($N = 1200$, $p > 0.05$). (c) Distribution of θ_{in} of the three collision results under different conditions. A two-way ANOVA analysis was conducted, and no significant difference was detected ($N = 1200$, $p > 0.05$).
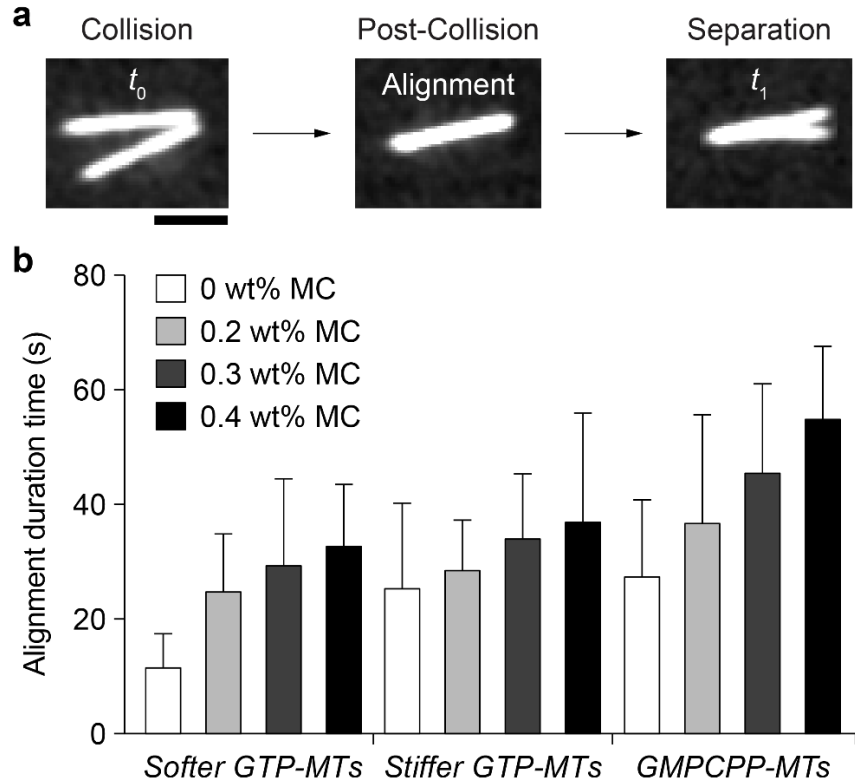
Figure 6. Durability of the aligned bundles increases with longer L_p of MTs and larger depletion force induced by a higher concentration of MC. (a) Alignment duration time is defined as the period between the moment of collision (t_0) and the moment of separation after alignment (t_1). Scale bar, 5μm. (b) Comparison of the alignment duration time among the three MT groups with different concentrations of MC. A two-way ANONA analysis was conducted, and an extremely significant difference was detected ($N = 160$, $p < 0.0001$).
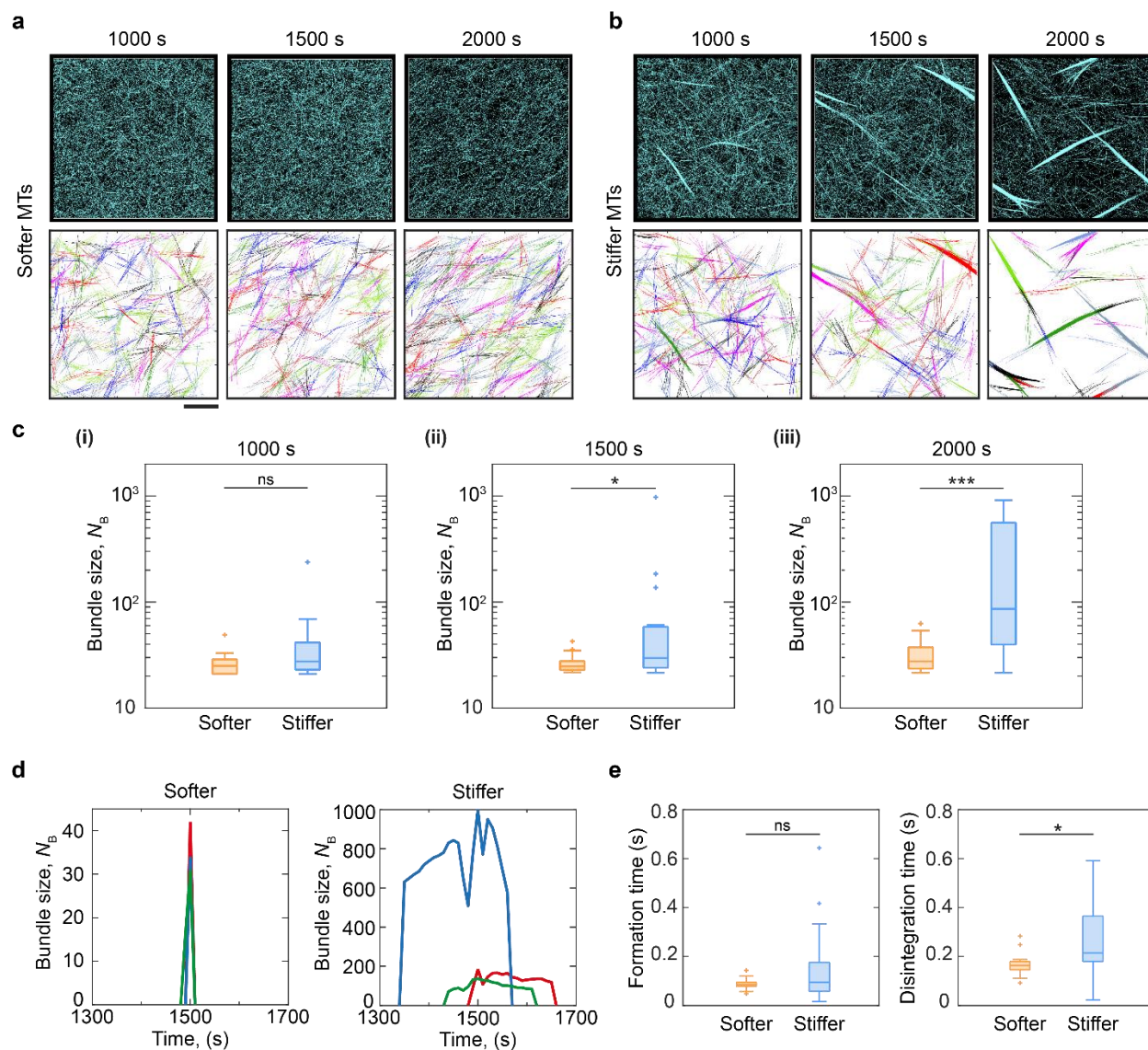
Figure 7. Computational model validates that the L_p-dependent durability of MT alignment dominates the bundle formation. (a) Collectively gliding softer MTs and (b) stiffer MTs in simulations at 1000 s, 1500 s, and 2000 s, respectively. Snapshots on the top row show all MT filaments in simulations. Plots at the bottom row show bundles identified by the number of filaments (bundle size) greater than 20. Stiffer MTs tend to align and aggregate to form dense and long-standing bundles, which are absent in the softer MT group. Scale bar = 20 μm. (c) Comparison of the bundle size between the softer and stiffer MT groups at (i) 1000 s; (ii) 1500 s; and (iii) 2000 s. Box plot with the whiskers extended to 1.5 of interquartile range to remove extreme outliers. The main box covers the upper to lower quartiles while the median value is represented by the horizontal line. A two-tailed Mann-Whitney-Wilcoxon test was conducted (ns: $p > 0.05$; *: $p < 0.05$; ***: $p < 0.001$) (d) Time course of the size of bundles detected at 1500 s in the softer and stiffer MT groups. Three individual bundles from softer and stiffer MT groups are plotted in red, green, and blue, respectively. (e) The formation and disintegration time of bundles calculated at 1500 s in the softer and stiffer MT groups. The time was normalized by

dividing with the bundle size N_B. A two-tailed Mann-Whitney-Wilcoxon test was conducted (ns: $p > 0.05$; *: $p < 0.05$).

ASSOCIATED CONTENT

The Supporting Information is available online.

Supporting Information. Supplementary Text, including (1) Model for classifying images, (2) Visualization of the classification strategy, (3) Brownian dynamics, (4) Propelling force and (5) Quantification of bundle dynamics in simulation, Figures S1–S6, Tables S1–S7, complete captions for Movies S1–S6, and Supplementary References (PDF).

Movie S1. Evolution process of the collective motion of *softer GTP-MTs* in the presence of 0.3 wt% MC. Scale bar = 50 μm. (MP4)

Movie S2. Evolution process of the collective motion of *stiffer GTP-MTs* in the presence of 0.3 wt% MC. Scale bar = 50 μm. (MP4)

Movie S3. Evolution process of the collective motion of *GMPCPP-MTs* in the presence of 0.3 wt% MC. Scale bar = 50 μm. (MP4)

Movie S4. Crossover of two MTs after a binary collision. Scale bar = 5 μm. (MP4)

Movie S5. Parallel alignment of two MTs after a binary collision. Scale bar = 5 μm. (MP4)

Movie S6. Anti-parallel alignment of two MTs after a binary collision. Scale bar = 5 μm. (MP4)

Author Contributions

H.Z., T.I.F., T.K. and R.Y. designed the experiments; H.Z. and T.I.F. performed the experiments and analyzed the data; W.J. and T.K. conducted the numerical simulation; all authors discussed, interpreted the results, and wrote the manuscript. All the authors approved the final version of the manuscript.

Notes

Authors declare that they have no competing interests.

REFERENCES

(1)   Vicsek, T.; Zafeiris, A. Collective Motion. *Phys. Rep.* **2012**, 517 (3–4), 71–140.

(2)   Filella, A.; Nadal, F.; Sire, C.; Kanso, E.; Eloy, C. Model of Collective Fish Behavior with Hydrodynamic Interactions. *Phys. Rev. Lett.* **2018**, 120 (19), 198101.

(3)   Dombrowski, C.; Cisneros, L.; Chatkaew, S.; Goldstein, R. E.; Kessler, J. O. Self-Concentration and Large-Scale Coherence in Bacterial Dynamics. *Phys. Rev. Lett.* **2004**, 93 (9), 098103.

(4)   Kawaguchi, K.; Kageyama, R.; Sano, M. Topological Defects Control Collective Dynamics in Neural Progenitor Cell Cultures. *Nature* **2017**, 545 (7654), 327–331.

(5)   Czirók, A.; Ben-Jacob, E.; Cohen, I.; Vicsek, T. Formation of Complex Bacterial Colonies via Self-Generated Vortices. *Phys. Rev. E* **1996**, 54 (2), 1791–1801.

(6)   Fletcher, D. A.; Mullins, R. D. Cell Mechanics and the Cytoskeleton. *Nature* **2010**, 463 (7280), 485–492.

(7)   Sanchez, T.; Chen, D. T. N.; DeCamp, S. J.; Heymann, M.; Dogic, Z. Spontaneous Motion in Hierarchically Assembled Active Matter. *Nature* **2012**, 491 (7424), 431–434.

(8)   Roeles, J.; Tsiavaliaris, G. Actin-Microtubule Interplay Coordinates Spindle Assembly in Human Oocytes. *Nat. Commun.* **2019**, 10 (1), 4651.

(9)   Hyman, A. A.; Karsenti, E. Morphogenetic Properties of Microtubules and Mitotic Spindle Assembly. *Cell* **1996**, 84 (3), 401–410.

(10)   Surrey, T.; Nédélec, F.; Leibler, S.; Karsenti, E. Physical Properties Determining Self-Organization of Motors and Microtubules. *Science* **2001**, 292 (5519), 1167–1171.

(11)   Doostmohammadi, A.; Ignés-Mullol, J.; Yeomans, J. M.; Sagués, F. Active Nematics. *Nat. Commun.* **2018**, 9 (1), 3246.

(12)   M. Lemma, L.; J. DeCamp, S.; You, Z.; Giomi, L.; Dogic, Z. Statistical Properties of Autonomous Flows in 2D Active Nematics. *Soft Matter* **2019**, 15 (15), 3264–3272.

(13)   Schaller, V.; Weber, C.; Semmrich, C.; Frey, E.; Bausch, A. R. Polar Patterns of Driven Filaments. *Nature* 2010, **467** (7311), 73–77.

(14)   Liu, L.; Tüzel, E.; Ross, J. L. Loop Formation of Microtubules during Gliding at High Density. *J. Phys. Condens. Matter* **2011**, 23 (37), 374104.

(15)   Inoue, D.; Mahmot, B.; Rashedul Kabir, A. M.; Ishrat Farhana, T.; Tokuraku, K.; Sada, K.; Konagaya, A.; Kakugo, A. Depletion Force Induced Collective Motion of Microtubules Driven by Kinesin. *Nanoscale* **2015**, 7 (43), 18054–18061.

(16)   Sumino, Y.; Nagai, K. H.; Shitaka, Y.; Tanaka, D.; Yoshikawa, K.; Chaté, H.; Oiwa, K. Large-Scale Vortex Lattice Emerging from Collectively Moving Microtubules. *Nature* **2012**, 483 (7390), 448–452.

(17)   Kakugo, A.; Tamura, Y.; Shikinaka, K.; Yoshida, M.; Kawamura, R.; Furukawa, H.; Osada, Y.; Gong, J. P. Formation of Well-Oriented Microtubules with Preferential Polarity in a Confined Space under a Temperature Gradient. *J. Am. Chem. Soc.* **2009**, 131 (50), 18089–18095.

(18)   Wada, S.; Kabir, A. Md. R.; Kawamura, R.; Ito, M.; Inoue, D.; Sada, K.; Kakugo, A. Controlling the Bias of Rotational Motion of Ring-Shaped Microtubule Assembly. *Biomacromolecules* **2015**, 16 (1), 374–378.

(19)   Isozaki, N.; Shintaku, H.; Kotera, H.; Hawkins, T. L.; Ross, J. L.; Yokokawa, R. Control of Molecular Shuttles by Designing Electrical and Mechanical Properties of Microtubules. *Sci. Robot.* **2017**, 2 (10).

(20)   Van den Heuvel, M. G. L.; Bolhuis, S.; Dekker, C. Persistence Length Measurements from Stochastic Single-Microtubule Trajectories. *Nano Lett.* **2007**, 7 (10), 3138–3144.

(21)   Van den Heuvel, M. G. L.; Graaff, M. P. de; Dekker, C. Microtubule Curvatures under Perpendicular Electric Forces Reveal a Low Persistence Length. *Proc. Natl. Acad. Sci. U.S.A.* **2008**, 105 (23), 7941–7946.

(22)   Schuldt, C.; Schnauß, J.; Händler, T.; Glaser, M.; Lorenz, J.; Golde, T.; Käs, J. A.; Smith, D. M. Tuning Synthetic Semiflexible Networks by Bending Stiffness. *Phys. Rev. Lett.* **2016**, *117* (19), 197801.

(23)   Tassieri, M. Dynamics of Semiflexible Polymer Solutions in the Tightly Entangled Concentration Regime. *Macromolecules* **2017**, *50* (14), 5611–5618.

(24)   Vicsek, T.; Czirók, A.; Ben-Jacob, E.; Cohen, I.; Shochet, O. Novel Type of Phase Transition in a System of Self-Driven Particles. *Phys. Rev. Lett.* **1995**, 75 (6), 1226–1229.

(25)   Peruani, F.; Klauss, T.; Deutsch, A.; Voss-Boehme, A. Traffic Jams, Gliders, and Bands in the Quest for Collective Motion of Self-Propelled Particles. *Phys. Rev. Lett.* **2011**, 106 (12), 128101.

(26)   Baskaran, A.; Marchetti, M. C. Hydrodynamics of Self-Propelled Hard Rods. *Phys. Rev. E* **2008**, 77 (1), 011920.

(27)   Ginelli, F.; Peruani, F.; Bär, M.; Chaté, H. Large-Scale Collective Properties of Self-Propelled Rods. *Phys*. *Rev*. *Lett*. **2010**, 104 (18), 184502.

(28)   Kraikivski, P.; Lipowsky, R.; Kierfeld, J. Enhanced Ordering of Interacting Filaments by Molecular Motors. *Phys. Rev. Lett.* **2006**, 96 (25), 258103.

(29)   Duman, Ö.; E. Isele-Holder, R.; Elgeti, J.; Gompper, G. Collective Dynamics of Self-Propelled Semiflexible Filaments. *Soft Matter* **2018**, 14 (22), 4483–4494.

(30)   Vliegenthart, G. A.; Ravichandran, A.; Ripoll, M.; Auth, T.; Gompper, G. Filamentous Active Matter: Band Formation, Bending, Buckling, and Defects. *Sci. Adv.* **2020**, 6 (30), eaaw9975.

(31)   Moore, J. M.; Thompson, T. N.; Glaser, M. A.; Betterton, M. D. Collective Motion of Driven Semiflexible Filaments Tuned by Soft Repulsion and Stiffness. *Soft Matter* **2020**, 16 (41), 9436–9442.

(32)   Hawkins, T.; Mirigian, M.; Selcuk Yasar, M.; Ross, J. L. Mechanics of Microtubules. *J. Biomech.* **2010**, 43 (1), 23–30.

(33)   Janson, M. E.; Dogterom, M. A Bending Mode Analysis for Growing Microtubules: Evidence for a Velocity-Dependent Rigidity. *Biophys. J.* **2004**, 87 (4), 2723–2736.

(34)   Schaedel, L.; John, K.; Gaillard, J.; Nachury, M. V.; Blanchoin, L.; Théry, M. Microtubules Self-Repair in Response to Mechanical Stress. *Nat. Mater.* **2015**, 14 (11), 1156–1163.

(35)   Zhou, H.; Isozaki, N.; Fujimoto, K.; Yokokawa, R. Growth Rate-Dependent Flexural Rigidity of Microtubules Influences Pattern Formation in Collective Motion. *J. Nanobiotechnol.* **2021**, 19 (1), 218.

(36)   Wang, H.; Wang, Z.; Du, M.; Yang, F.; Zhang, Z.; Ding, S.; Mardziel, P.; Hu, X. Score-CAM: Score-Weighted Visual Explanations for Convolutional Neural Networks. In *2020*

IEEE/CVF Conference on Computer Vision and Pattern Recognition Workshops (CVPRW); Seattle, WA, USA, June 14-19, 2020; Lisa O'Conner, Ed.; IEEE: Los Alamitos, **2020**; pp 111–119

(37)   Suzuki, R.; Bausch, A. R. The Emergence and Transient Behaviour of Collective Motion in Active Filament Systems. *Nat. Commun.* **2017**, 8 (1), 41.

(38)   Higaki, T. Quantitative Evaluation of Cytoskeletal Organizations by Microscopic Image Analysis. *Plant Morphol.* **2017**, 29 (1), 15–21.

(39)   Farhadi, L.; Fermino Do Rosario, C.; Debold, E. P.; Baskaran, A.; Ross, J. L. Active Self-Organization of Actin-Microtubule Composite Self-Propelled Rods. *Front. Phys.* **2018**, 6, 75.

(40)   Saito, A.; Ishrat Farhana, T.; Rashedul Kabir, A. M.; Inoue, D.; Konagaya, A.; Sada, K.; Kakugo, A. Understanding the Emergence of Collective Motion of Microtubules Driven by Kinesins: Role of Concentration of Microtubules and Depletion Force. *RSC Adv.* **2017**, 7 (22), 13191–13197.

(41)   Kim, K.; Yoshinaga, N.; Bhattacharyya, S.; Nakazawa, H.; Umetsu, M.; Teizer, W. Large-Scale Chirality in an Active Layer of Microtubules and Kinesin Motor Proteins. *Soft Matter* **2018**, 14 (17), 3221–3231.

(42)   Tharmann, R.; Claessens, M. M. A. E.; Bausch, A. R. Micro- and Macrorheological Properties of Actin Networks Effectively Cross-Linked by Depletion Forces. *Biophys. J.* **2006**, 90 (7), 2622–2627.

(43)   Tokuraku, K.; Matsushima, K.; Matui, T.; Nakagawa, H.; Katsuki, M.; Majima, R.; Kotani, S. The Number of Repeat Sequences in Microtubule-Associated Protein 4 Affects the Microtubule Surface Properties. *J. Biol. Chem.* **2003**, 278 (32), 29609–29618.

(44)   Takatsuki, H.; Bengtsson, E.; Månsson, A. Persistence Length of Fascin-Cross-Linked Actin Filament Bundles in Solution and the in Vitro Motility Assay. *Biochim. Biophys. Acta. Gen. Subj.* **2014**, *1840* (6), 1933–1942.

(45)   Duke, T.; Holy, T. E.; Leibler, S. "Gliding Assays" for Motor Proteins: A Theoretical Analysis. *Phys. Rev. Lett.* **1995**, *74* (2), 330–333.

(46)   Nitta, T.; Hess, H. Dispersion in Active Transport by Kinesin-Powered Molecular Shuttles. *Nano Lett.* **2005**, *5* (7), 1337–1342.

(47)   Sweet, M.; Kang'iri, S. M.; Nitta, T. Linking Path and Filament Persistence Lengths of Microtubules Gliding over Kinesin. *Sci. Rep.* **2022**, *12* (1), 3081.

(48)   Gibbons, F.; Chauwin, J.-F.; Despósito, M.; José, J. V. A Dynamical Model of Kinesin-Microtubule Motility Assays. *Biophys. J.* **2001**, *80* (6), 2515–2526.

(49)   Kerssemakers, J.; Ionov, L.; Queitsch, U.; Luna, S.; Hess, H.; Diez, S. 3D Nanometer Tracking of Motile Microtubules on Reflective Surfaces. *Small* **2009**, 5 (15), 1732–1737.

(50) Liu, L.; Tüzel, E.; Ross, J. L. Loop Formation of Microtubules during Gliding at High Density. *J. Phys. Condens. Matter* **2011**, *23* (37), 374104.

(51) Bassir Kazeruni, N. M.; Rodriguez, J. B.; Saper, G.; Hess, H. Microtubule Detachment in Gliding Motility Assays Limits the Performance of Kinesin-Driven Molecular Shuttles. *Langmuir* **2020**, 36 (27), 7901–7907.

(52) Bourdieu, L.; Duke, T.; Elowitz, M. B.; Winkelmann, D. A.; Leibler, S.; Libchaber, A. Spiral Defects in Motility Assays: A Measure of Motor Protein Force. *Phys. Rev. Lett.* **1995**, 75 (1), 176–179.

(53) Köhler, S.; Lieleg, O.; Bausch, A. R. Rheological Characterization of the Bundling Transition in F-Actin Solutions Induced by Methylcellulose. *PLoS One* **2008**, 3 (7), e2736.

(54) Svoboda, K.; Block, S. M. Force and Velocity Measured for Single Kinesin Molecules. *Cell* **1994**, 77 (5), 773–784.

(55) Blehm, B. H.; Schroer, T. A.; Trybus, K. M.; Chemla, Y. R.; Selvin, P. R. In Vivo Optical Trapping Indicates Kinesin's Stall Force Is Reduced by Dynein during Intracellular Transport. *Proc. Natl. Acad. Sci. U.S.A.* **2013**, 110 (9), 3381–3386.

(56) Yang, Y.; Turci, F.; Kague, E.; Hammond, C. L.; Russo, J.; Royall, C. P. Dominating Length scales of Zebrafish Collective Behaviour. *PLoS Comput. Biol.* **2022**, *18* (1), e1009394.

(57) Chaté, H.; Ginelli, F.; Grégoire, G.; Raynaud, F. Collective Motion of Self-Propelled Particles Interacting without Cohesion. *Phys. Rev. E* **2008**, *77* (4), 046113.

(58) Ginelli, F. The Physics of the Vicsek Model. *Eur. Phys. J.: Spec. Top.* **2016**, *225* (11–12), 2099–2117.

(59) Castoldi, M.; Popov, A. V. Purification of Brain Tubulin through Two Cycles of Polymerization–Depolymerization in a High-Molarity Buffer. *Protein Expr. Purif.* **2003**, 32 (1), 83–88.

(60) Yokokawa, R.; Tarhan, M. C.; Kon, T.; Fujita, H. Simultaneous and Bidirectional Transport of Kinesin-Coated Microspheres and Dynein-Coated Microspheres on Polarity-Oriented Microtubules. *Biotechnol. Bioeng.* **2008**, 101 (1), 1–8.

(61) Wiggins, C. H.; Riveline, D.; Ott, A.; Goldstein, R. E. Trapping and Wiggling: Elastohydrodynamics of Driven Microfilaments. *Biophys. J.* **1998**, *74* (2), 1043–1060.

(62) Liu, Z.-Q. Scale Space Approach to Directional Analysis of Images. *Appl. Opt.* **1991**, 30 (11), 1369–1373.

(63) Ozawa, K.; Taomori, H.; Hoshida, M.; Kunita, I.; Sakurazawa, S.; Honda, H. Millimeter-Sized Belt-like Pattern Formation of Actin Filaments in Solution by Interacting with Surface Myosin in Vitro. *Biophys. Physicobiol.* **2019**, 16, 1–8.

(64) Arganda-Carreras, I.; Fernández-González, R.; Muñoz-Barrutia, A.; Ortiz-De-Solorzano, C. 3D Reconstruction of Histological Sections: Application to Mammary Gland Tissue. *Microsc. Res. Tech.* **2010**, 73 (11), 1019–1029.

(65) Liberzon, A.; Käufer, T.; Bauer, A.; Vennemann, P.; Zimmer, E. *OpenPIV/Openpiv-Python*, version 0.23.6; Zenodo: Geneve, **2021**.

TABLE OF CONTENTS GRAPHIC